This is a preprint of the following article, which is available from http://mdolab.engin.umich.edu
Gustavo L. O. Halila, Krzysztof J. Fidkowski, Joaquim R. R. A. Martins, Toward Automatic PSE-based Transition to Turbulence Prediction for Aerodynamic Flows. *AIAA Journal*, 2020.
The published article may differ from this preprint, and is available by following the DOI: https://doi.org/10.2514/1.J059516.

Toward Automatic PSE-based Transition to Turbulence Prediction for Aerodynamic Flows

Gustavo L. O. Halila, Krzysztof J. Fidkowski, Joaquim R. R. A. Martins
Department of Aerospace Engineering, University of Michigan, Ann Arbor, MI, 48109

Abstract

The inclusion of transition-to-turbulence effects in Computational Fluid Dynamics (CFD) simulations is essential to accurately predict drag reduction from the use of laminar flow technologies. The parabolized stability equations (PSE) method takes into account nonlocal and nonparallel effects on boundary layer dynamics. Its computational cost compares to that of linear stability theory (LST) analysis, which does not account for these effects. However, difficulties related to the robustness of PSE have prevented its application to industrial cases, where the more straightforward LST approach has been adopted because of its relative ease of use. When using PSE with an e^N transition method, it is necessary to determine the stability modes that trigger transition and their neutral points. We propose a robust PSE-based transition framework that includes a boundary layer solver, a database method, and an LST solver that provides the required stability modes and the corresponding neutral points so that a robust PSE calculation is automatically performed. Our approach leverages an automatic framework for the application of PSE-based transition prediction to aerodynamic flow analysis.

Nomenclature

$\mathbf{A}$, $\mathbf{B}$, $\mathbf{C}$, $\mathbf{D}$	=	Flow stability matrix operators
$E(x)$	=	$\frac{1}{2}\int_0^\infty (\lvert\hat{\mathbf{u}}\rvert^2 + \lvert\hat{\mathbf{v}}\rvert^2 + \lvert\hat{\mathbf{w}}\rvert^2)\, dy$, disturbance kinetic energy
f	=	Dimensional frequency (Hz)
F	=	ω_r / Re_{δ_1}, reduced frequency
h_x, h_y	=	Curvature metrics
H_{12}	=	Boundary layer shape factor
i	=	$\sqrt{-1}$, imaginary number

N	=	$\ln(A/A_0)$, amplification factor
N_{crit}	=	Critical amplification factor
$\mathbf{q}$	=	(ρ, u, v, w, T), flow state vector
$\bar{\mathbf{q}}$	=	Steady, base flow state vector
$\tilde{\mathbf{q}}$	=	Unsteady, disturbance state vector
$\hat{\mathbf{q}}$	=	Disturbance amplitude state vector
Re	=	$U_e\delta(x)/\nu$, local Reynolds number based on the characteristic length scale
Tu	=	Freestream turbulence intensity
x	=	Coordinate in the streamwise direction
y	=	Coordinate in the wall-normal direction
z	=	Coordinate in the spanwise direction
$\hat{\mathbf{u}}$	=	Disturbance velocity amplitude vector
u	=	Velocity component in the streamwise direction
v	=	Velocity component in the spanwise direction
w	=	Velocity component in the wall-normal direction
α	=	Streamwise wave number
$-\alpha_i$	=	Disturbance growth rate in the local, parallel stability problem
β	=	Spanwise wave number
δ	=	$\sqrt{\nu x/U_e}$, characteristic length scale
δ_1	=	Boundary layer displacement thickness
δ_2	=	Boundary layer momentum thickness
ϵ	=	Linear perturbation amplitude factor
ω	=	Angular frequency
Θ	=	Phase function
σ	=	Disturbance growth rate
σ_E	=	Disturbance kinetic energy based growth rate

Subscripts

0	=	Neutral point location
1	=	Initial marching location
e	=	Boundary layer edge
E	=	Energy
i	=	Imaginary part
NP	=	Neutral point
p, l	=	PSE-based, local, parallel
r	=	Real part

1 Introduction

In airplane aerodynamic design, the inclusion of transition-to-turbulence effects into the computational fluid dynamics (CFD) process allows the aerodynamicist to explore the benefits of laminar flow airframes, which leads to lower-drag airplanes. Laminar flow aircraft concepts (both natural and active) have recently gained traction as a

means to reduce airframe drag [1–3] Predictive computational fluid dynamics (CFD) models for laminar to turbulent flow transition are needed to design and optimize such concepts. Typical jetliners have a drag breakdown at cruise in which around 55% of the total drag comes from viscous effects [4]. Turbulent boundary layers present a larger momentum transfer in the wall-normal direction when compared to laminar boundary layers, and therefore, the velocity profiles are fuller in the former [5]. As a consequence, the skin friction coefficient is larger in turbulent boundary layers, leading to increased viscous drag for turbulent, wall-bounded flows. Lower drag through laminar flow technology means reduced fuel consumption and greenhouse gas emissions. A significant portion of the direct operational cost (DOC) is attributable to fuel consumption and, therefore, laminar flow technology is a valuable asset in modern airplane design. Beyond laminar flow technology applications, including transition-to-turbulence effects improves computational results for conventional airframes. As an example, high-lift devices typically present small Reynolds numbers in slats and flaps, and, therefore, transition-to-turbulence should be included to improve the comparisons of numerical results to experimental data, and to improve flight performance predictions [6].

Transition to turbulence starts with the receptivity of external disturbances in the laminar boundary layer. These disturbances can be caused by surface roughness, waviness, steps and gaps, freestream turbulence, and acoustic noise. Different routes leading to turbulence are possible, all originating in the receptivity process mentioned above. For aircraft at cruise conditions, two paths are the most common ways to originate turbulence. The receptivity mechanisms may give rise to instabilities that, at first, present an exponential growth, also called modal growth. In this scenario, Tollmien–Schlichting (TS) waves, both traveling and stationary crossflow (CF) disturbances, and Görtler vortices are considered. Eventually, these initially amplifying modes lead to nonlinear effects followed by breakdown to turbulence. This is the most common path to turbulence when low turbulence levels are present, as in cruise flight conditions and quiet wind tunnels. A complete review of the process outlined above is available in the literature [7, 8]. In a second possible route to turbulence, all the linear effects are bypassed, and the so-called bypass mechanism leads to turbulence breakdown directly. This path takes place in high freestream turbulence environments or, in the case of free flight conditions, in the scenario where the turbulent wake of one element of the airframe interacts with a second airframe element, bypassing the exponential growth stage in the second element.

Different linear stability methods have been proposed for engineering transition to turbulence prediction [9]. The first practical transition prediction tools date back to the work of Smith and Gamberoni [10] and van Ingen [11], with the use of an e^N method.

The Orr–Sommerfeld equation, assuming a parallel base flow without boundary layer history effects, served as the basis for the linear stability theory (LST) approach. Some of the drawbacks of this approach are the lack of boundary layer history effects, as well as nonparallel effects that characterize boundary layer flows. In addition, it is not consistent to include curvature effects into LST simulations since, for airfoils and wings, they are typically of the order of magnitude of the terms ignored in the formulation [12].

To better represent the physics of transition in boundary layer flows, the inclusion of nonparallel, nonlocal, and curvature effects was considered by Bertolotti and Herbert [13]. The method, based on the parabolization of the Linearized Navier–Stokes (LNS) equations, is referred to as parabolized stability equations (PSE). One attractive aspect of the PSE approach is that, in its linear version, the computational cost is of the same order as that of LST computations [12]. When the technique first appeared in the early 1990s, it was expected that it would be used as an engineering tool to perform transition-to-turbulence prediction [14]. However, despite its improved agreement with experiments and low computational cost, the PSE approach has not been broadly adopted for engineering applications [15]. There are several reasons for this. First, the correct computation of N-envelopes using the PSE approach depends on the knowledge of the neutral point location for each of the wave modes considered in the integration procedure [16]. Second, the estimation of the stability modes to be considered to form the N-envelope is not necessarily straightforward and may be computationally expensive. It is known that, depending on the mode generation strategy, spurious wave modes that lead to unbounded amplification may be included in the PSE computation. Industrial practices favor computational methods that can be automated with little user intervention, whereas PSE methods are currently mostly used by expert users in custom research environments. The lack of literature on how to perform the PSE initialization in an efficient, automatic way is an obstacle in the use of nonlocal, nonparallel flow stability tools in industrial environments. Among the few investigations on PSE-based transition prediction for industrial applications available in the literature, the work of Kosarev et al. [15] suggests a procedure to automate the solution from the linear stability problem needed to initiate the PSE computations in the first marching station. To this end, the authors introduced an inflow empirical correlation. However, information on the flow stability modes that should be selected to perform the N-envelope computation is not provided.

To address the issues mentioned above, we propose a robust, automatic PSE-based transition prediction framework. The novelty of our approach lies in the efficient coupling of a database method [17], an LST code [18], and a PSE solver. Based on the boundary layer characteristics, a two-entry look-up table that uses results obtained with the database method suggests a set of waves to be used in the transition to turbulence analysis, including both TS waves and CF vortices. For the former, following the suggestion of Krumbein [19], we focus on TS waves that are aligned with the external streamline direction. This is valid because, in typical flight situations, the TS waves of interest do not deviate from the inviscid streamline significantly. After the set of initial modes is determined by the database method, the LST tool starts a computation inside the unstable region, marching upstream until the lower branch of the neutral curve is crossed, indicating the neutral point location. With information on the modes and neutral points, the PSE tool is automatically initiated. In the present work, we restrict ourselves to the study of transition to turbulence triggered by TS wave amplification. The effects of CF mode amplification, which are currently included in the mode initialization and PSE computation processes, will be addressed in a future study. We also provide information on discretization, domain size selection, mesh refinement, and other relevant aspects related to a robust PSE implementation.

We present airfoil transitional flow results, including an in-depth analysis of the stability modes involved. We believe that the present framework serves as a step towards the use of the PSE technique in engineering applications.

This paper is organized as follows. Section 2 provides an overview of the PSE formulation. The complete PSE-based transition prediction framework, including implementation details, is discussed in Sec. 3. Section 4 presents numerical results for the NLF(1)-0416 airfoil and Sec. 5 concludes the paper with final remarks.

2 Parabolized Stability Equations

In modal linear stability theory, the stability problem is solved by using a set of wave modes, each of which is solved independently. Both PSE and LST are examples of modal linear stability methods. The overall principle is based on the decomposition of the flow state vector $\mathbf{q}$ into a steady base flow state $\bar{\mathbf{q}}$ and an unsteady perturbation component, $\tilde{\mathbf{q}}$. The decomposition reads $\mathbf{q}(\mathbf{x},t) = \bar{\mathbf{q}}(\mathbf{x}) + \epsilon\tilde{\mathbf{q}}(\mathbf{x},t)$, where $\mathbf{x}$ is the space coordinate vector, t is the time, and $\mathbf{q} = (\rho, u, w, v, T)$ is the flow state vector, and $\epsilon \ll 1$.

The PSE method is appropriate for the analysis of streamwise disturbance growth in slowly varying shear flows such as boundary layers [13, 14, 20]. Mathematically, this is expressed as

$$\partial_x \bar{\mathbf{q}} \ll \partial_y \bar{\mathbf{q}}; \quad \partial_z \bar{\mathbf{q}} = \mathbf{0}, \tag{1}$$

$$\bar{\mathbf{q}}(\mathbf{x}) = \bar{\mathbf{q}}(x^*, y), \tag{2}$$

where x^* is a scaled version of x used to represent the base flow slow variation in the x direction.

The base flow velocity components $\bar{u}$ and $\bar{v}$, aligned with the streamwise and spanwise directions, respectively, exhibit small variations in the streamwise (x) direction and are constant along the spanwise (z) direction. We introduce the local Reynolds number, $Re = U_e\delta(x)/\nu$ where ν is the kinematic viscosity and $\delta(x)$ is a length scale proportional to the boundary layer thickness, $\delta(x) = \sqrt{\nu x/U_e}$, where U_e is the unperturbed boundary layer edge velocity. The length scale, $\delta(x)$, is typically used in PSE analysis [21, 22]. The reference length scale used to nondimensionalize the equations is δ evaluated at the first marching streamwise coordinate [13]. The wall-normal component, $\bar{w}$, is nonzero and scales with $1/Re$. Formally defining the slowly varying scale $x^* = x/Re$, the scalings are:

$$\begin{aligned} \bar{w} &\sim \frac{1}{Re}, \\ \frac{\partial}{\partial x^*} &\sim \frac{1}{Re}, \\ \alpha &= \alpha\left(x^*\right), \\ \hat{\mathbf{q}} &= \hat{\mathbf{q}}\left(x^*, y\right). \end{aligned} \tag{3}$$

In a linear PSE analysis, the perturbation vector is expanded in terms of a single

mode, truncated Fourier component assuming time-periodicity,

$$\tilde{\mathbf{q}}(x,y,x,t) = \hat{\mathbf{q}}(x,y)\exp\left[i\left(\int_x \alpha\,(x')\,dx' + \beta z - \omega t\right)\right], \tag{4}$$

where $\hat{\mathbf{q}}(x,y)$ has a slow variation in x. The flow disturbance amplitudes, $\hat{\mathbf{q}}$, present the three velocity components even when a two-dimensional base flow is considered.

To obtain the linear PSE equations, we replace the flow state vector decomposition, $\mathbf{q}(\mathbf{x},t) = \bar{\mathbf{q}}(\mathbf{x}) + \epsilon\tilde{\mathbf{q}}(\mathbf{x},t)$, in the linearized Navier–Stokes equations and neglect terms of $\mathcal{O}(\epsilon^2)$. We also consider the scaling from Eq. (3) and neglect higher derivatives with respect to x in the viscous terms (noting that $\frac{\partial}{\partial x}\frac{1}{Re} \sim \epsilon^2$). The resulting linear PSE equations, in compact form, read

$$\mathbf{A}\hat{\mathbf{q}} + \mathbf{B}\frac{1}{h_y}\frac{\partial\hat{\mathbf{q}}}{\partial y} + \mathbf{C}\frac{1}{h_y^2}\frac{\partial^2\hat{\mathbf{q}}}{\partial y^2} + \mathbf{D}\frac{1}{h_x}\frac{\partial\hat{\mathbf{q}}}{\partial x} = \mathbf{0}, \tag{5}$$

where h_x and h_y are curvature metrics. The entries for the compressible PSE operators $\mathbf{A}$, $\mathbf{B}$, $\mathbf{C}$, and $\mathbf{D}$ are detailed by Hanifi et al. [21]. The boundary conditions are:

$$\hat{u} = \hat{v} = \hat{w} = \hat{T} = 0 \quad \text{at} \quad y = 0, \tag{6}$$

$$\hat{u} = \hat{v} = \hat{w} = \hat{T} = 0 \quad \text{as} \quad y \to \infty. \tag{7}$$

In the PSE framework, changes in amplitude along the slowly varying spatial direction are contained both in the amplitude function $\hat{\mathbf{q}}$ and in the phase function defined in Eq. (4). To remove such ambiguity, a normalization condition is required. One possibility for the normalization is to impose that the total kinetic energy of the shape function be independent of x so that fast disturbance variations in the streamwise direction are absorbed into the phase function [14],

$$\int_0^\infty \hat{\mathbf{u}}^\dagger \frac{\partial\hat{\mathbf{u}}}{\partial x} dy = 0, \tag{8}$$

where the superscript † represents the complex conjugate. This normalization condition also ensures an assumed scaling of $\partial\hat{\mathbf{q}}/\partial x$ with $1/Re$. The disturbance kinetic energy is used to measure the disturbance growth,

$$E(x) = \frac{1}{2}\int_0^\infty \left(|\hat{\mathbf{u}}|^2 + |\hat{\mathbf{v}}|^2 + |\hat{\mathbf{w}}|^2\right) dy. \tag{9}$$

The disturbance kinetic energy-based disturbance growth ratio reads

$$\sigma_E = \frac{1}{h_x}\left(-\alpha_i + \frac{d}{dx}\ln\sqrt{E(x)}\right). \tag{10}$$

The linear PSE (5) are intended to be parabolic. Therefore, it is possible to treat the streamwise direction as a pseudo-time and then to implement a marching strategy in this spatial direction. Numerical instabilities appear when the streamwise integration step is too small [22]. The reason for that, as explained by Herbert [14], is that

there are traces of ellipticity that inject ill-posed characteristics. One remedy for this is the use of a first-order backward difference scheme with a lower integration step limit $\Delta x > 1/|\alpha_r|$. To relax this limit, Andersson et. al. [23] propose a stabilization procedure leading to $\Delta x > 1/|\alpha_r| - 2s$, where s is a small number.

When three-dimensional base flows are considered, there are some possibilities for the marching direction. Using an orthogonal coordinate system, the most common approach is to orient the streamwise direction towards a normal to the leading edge, where the spanwise direction is parallel to the leading edge. [24] Another choice would be to perform a marching that follows the inviscid streamline. A complete discussion on suitable marching directions is available in the literature [15, 25].

Due to the predominantly parabolic character of the linear PSE (5), the disturbance evolution is influenced by both local and upstream flow information and, therefore, the PSE method is recognized as a *nonlocal* approach, in contrast to, for instance, the Orr–Sommerfeld equation, which is a *local* formulation. We present details of an efficient PSE implementation oriented towards transition prediction in Sec. 3.4.

3 PSE-based Transition Prediction Framework

The boundary layer dynamics are governed by nonlocal, nonparallel effects. The PSE approach consists of a linear flow stability problem for a base flow configuration that considers these boundary layer dynamics. Lack of information on key numerical aspects in the literature is one of the factors that has prevented practicing engineers from employing the PSE method in transition prediction computations. Aspects such as neutral point location selection, effects of mesh refinement, marching initialization, and the choice of domain size have been neglected in previous studies. The present study includes information on these aspects and provides guidelines for a robust PSE-based transition prediction computation. When selecting modes for use in the N-envelope calculation, it is relevant to avoid or filter out spurious modes that could lead to unbounded amplification in the PSE computation.

The transition prediction framework based on the PSE computation combines the boundary layer solver, database method, linear stability theory (LST) solver, and the PSE solver itself. The PSE-based transition framework is illustrated in Fig. 1.

The pressure coefficient distribution from a RANS, Euler, or potential flow solver is used as the freestream boundary condition in the boundary layer solver. The boundary layer solver provides the base flow information required in the LST and PSE computations. The stability modes are computed using a database method that considers the base flow characteristics. The neutral point locations for the stability modes are computed by the LST solver. With base flow, wave modes, and neutral point information, the PSE computation is performed.

We introduce our boundary layer solver in Sec. 3.1. The database method is introduced in Sec. 3.2, while the LST solver and details on the PSE computation are presented in Secs. 3.3 and 3.4, respectively. The N-factor computation and transition onset estimation processes are illustrated in Sec. 3.5. We present further details on the complete transition framework in Sec. 3.6.

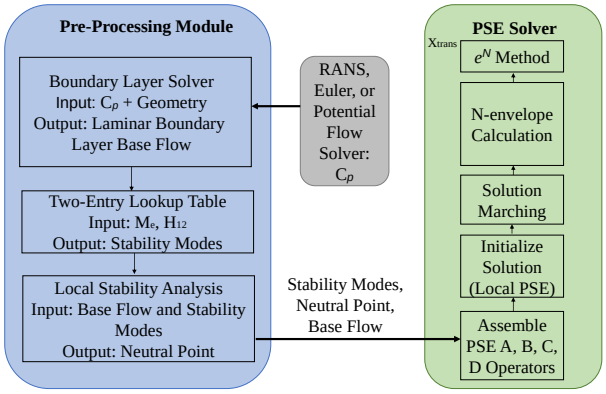

Figure 1: PSE-based transition prediction framework. The PSE code outputs the transition location.

3.1 Boundary Layer Solver

Our boundary layer solver considers a conical boundary layer topology. In the conical boundary layer assumption, $\partial p/\partial r = 0$, where r is the distance along the generator from a fictive origin [26]. Since we use a compressible formulation, the laminar boundary-layer system consists of the continuity, momentum, and energy equations, forming a system of parabolic partial differential equations [27].

The boundary layer governing equations are discretized using a second-order accurate, central-difference scheme in the wall normal direction [28]. The streamwise direction, which represents the marching direction, is discretized using a second-order backward finite difference scheme. We solve the nonlinear differential equations using Newton's method [29], where each Newton step is solved with the block-elimination method in this finite-difference solver [28].

Flow parameters such as the Mach and Reynolds numbers are used as inputs to the boundary layer solver. The freestream boundary condition is based on a pressure coefficient distribution. The boundary layer solver provides the displacement thickness, δ_1, the momentum thickness, δ_2, the boundary layer shape factor, H_{12}, the boundary layer velocity profiles and its derivatives in the streamwise and wall-normal directions. Shi et al. [28] provide further details on the boundary layer solver.

3.2 Database Method and Mode Selection

We use a two-entry lookup table based on the database method proposed by Arnal [30], which was further developed by Perraud et al. [17], and an LST implementation following the details presented by Shi et al. [18] to generate the stability modes that are used as the initial guess in the first PSE station. A PSE station corresponds to a discrete streamwise location.

The stability modes for a given base flow represented by the Mach number, M_e, and the boundary layer shape factor, H_{12}, are stored in a two-entry (M_e, H_{12}) lookup table that outputs the mode information (α, β, ω.) The database method is embedded in

the boundary layer solver described in Sec. 3.1. As will be further detailed in Sec. 3.4, we initialize the first station in the PSE calculation by solving a parallel, local problem based on the PSE operators. The angular frequency, ω, the streamwise wave number, α, and spanwise wave number, β, used in this initial section are provided by the two-entry lookup table. A deeper discussion on the database method and LST method can be found in previous work [28].

The mode generation process is based on the stability characteristics of a large number of three-dimensional Falkner–Skan–Cooke (FSC) similarity profiles [30]. The boundary layer states are computed based on the relation between the FSC auxiliary variable and a stream function. The stream function relates directly to the flow states. A detailed derivation of the FSC equations is available in the literature [5, 31].

The database method represents the local, parallel growth rate, $\sigma = -\alpha_i$, by a curve that envelopes two inverted parabolas. These parabolas mimic the dependency of α_i on the displacement thickness Reynolds number, Re_{δ_1}. The representation of $\sigma(Re_{\delta_1})$ is based on the maximum of two parabolas, one involving viscous effects, σ_V, and the other restricted to inviscid phenomena, σ_I. These two parabolas are functions of Re_{δ_1} and parameters that define the abscissa points where the parabolas intersect the Re_{δ_1} axis, R_K, and where σ reaches a maximum, R_M,

$$\sigma_I = \sigma_I \left(Re_{\delta_1}, R_{M_I}, R_{K_I} \right), \tag{11}$$

$$\sigma_V = \sigma_V \left(Re_{\delta_1}, R_{M_V}, R_{K_V} \right), \tag{12}$$

where the subscripts V and I denote, respectively, viscous and inviscid growth rates. A detailed derivation of the parabolas defined by Eqns. (11) and (12) is provided in by Perraud [17] and by Shi et al. [28]. The resulting envelope $\sigma = -\alpha_i$ obtained by the database method reads

$$\sigma_{DB} = \max \left(\sigma_I, \sigma_V \right). \tag{13}$$

To obtain the two-entry lookup table that provides the wave modes used in the PSE initialization, we start by solving the FSC equations and generate numerous similarity velocity profiles corresponding to different H_{12} values in the external streamline direction. We then run the LST code at specified M_e, H_{12}, and F and compute the exact, local, parallel amplification rate $\sigma = -\alpha_i$. The reduced frequency in the temporal framework, F, is defined as,

$$F = \frac{\omega_r}{Re_{\delta_1}}. \tag{14}$$

The boundary layer shape factor, H_{12}, is

$$H_{12} = \frac{\delta_1}{\delta_2}, \tag{15}$$

where δ_1 and δ_2 are, respectively, the boundary layer displacement and momentum thicknesses. We then compute σ_{DB} based on the database method for each specified M_e and H_{12} at different reduced frequencies. A least squares fitting process is used to obtain all the database method parameters, which are defined in the literature [17, 28], with different F at specified M_e and H_{12}. The least squares fitting also considers the

relation between σ_{DB}, from the database method estimate, and $-\alpha_i$, from the exact LST computations, for a range of base flows.

Finally, a two-entry lookup table for different M_e and H_{12} based on the database method parameters is established. The lookup table is constructed once, and therefore we only need to access it to obtain the required stability modes for a given base flow with Mach number M_e and boundary layer shape factor H_{12}. For a given base flow characterized by M_e and H_{12}, the results from the two-entry lookup table suggest a set of 20 TS waves and 20 CF vortices. The use of 20 modes for each mechanism results from numerical experimentation, which indicated that this quantity of modes was sufficient to accurately detect the transition onset point. The two-entry lookup table is valid for $2.22 < H_{12} < 4.023$ and $0 < M_e < 1.3$.

3.3 Linear Stability Theory

The linear stability theory (LST) approach considers a parallel, local base flow assumption and represents the solution of the Orr–Sommerfeld equation. As the nonlocal effects are not present, the streamwise base flow derivatives are not accounted for and the stability problem becomes an eigenvalue problem. Curvature effects are also not included since their effects are of the order of the terms neglected in the LST formulation [12]. The LST equation in compact form for compressible flows is expressed as,

$$\frac{d^2\hat{\mathbf{q}}}{dy^2} + \mathbf{A}_L \frac{d\hat{\mathbf{q}}}{dy} + \mathbf{B}_L \hat{\mathbf{q}} = \omega \mathbf{C}_L \hat{\mathbf{q}}, \tag{16}$$

where $\mathbf{A}_L$, $\mathbf{B}_L$, and $\mathbf{C}_L$ are the LST operators related to the base flow parameters and the wave numbers α and β [32]. This linear system of ordinary differential equations is described in detail by Cebeci [27]. Since different powers of α appear in the expressions that represent the spatial eigenvalue problem, it is advantageous to solve a temporal problem instead [14]. We use a fast algorithm of the Rayleigh quotient method [33] to solve the generalized eigenvalue problem in the temporal framework and apply the Gaster transformation [34] to obtain the spatial stability results needed to initialize the PSE method. In the spatial theory, the streamwise wavenumber, α, is a complex number, $\alpha = \alpha_r + i\alpha_i$, where the subscripts r and i denote the real and imaginary parts, respectively. The angular frequency, ω, is a real number. In the temporal framework, the streamwise wavenumber is real and the angular frequency is a complex number, $\omega = \omega_r + i\omega_i$. The Gaster transformation associates wave numbers as obtained in the temporal (subscript T) and spatial (subscript S) theories as follows

$$\alpha_{r,S} \approx \alpha_{r,T}, \tag{17}$$

$$\omega_{r,S} \approx \omega_{r,T}, \tag{18}$$

$$\frac{\omega_{i,T}}{\alpha_{i,S}} \approx -\frac{\partial \omega_r}{\partial \alpha_r}. \tag{19}$$

In the spatial framework, the parallel, local wave mode growth rate, σ, is equivalent to the imaginary part of the streamwise wavenumber with a switch in sign: $\sigma = -\alpha_i$. The neutral point corresponds to the position where the stability mode has zero growth

rate. It is possible to determine the neutral point location by starting a computation inside the unstable region, where $\alpha_i < 0$, and move upstream until $\alpha_i = 0$, defining the neutral point.

For each of the stability modes suggested by the database method, upstream marching is used to define the neutral point. The neutral point determination is illustrated in Algorithm 1. In Algorithm 1, the left arrow indicates an assignment. For instance, $x \leftarrow x_j$, indicates that the discrete streamwise position x_j is assigned to variable x.

Algorithm 1 Neutral point determination

for i **in** n_{modes} **do**
  for j **in** n_{stations} **do**
    if $\alpha_i < 0$ **then**
      $x \leftarrow x_j$ ▷ Initialize neutral point location when inside the unstable region
    end if
    while $\alpha_i < 0$ **do**
      $\frac{d^2\hat{\mathbf{q}}}{dy^2} + \mathbf{A}_L \frac{d\hat{\mathbf{q}}}{dy} + \mathbf{B}_L \hat{\mathbf{q}} = \omega \mathbf{C}_L \hat{\mathbf{q}}$ ▷ Solve the LST problem in the current flow station
      $x \leftarrow x_{j-1}$ ▷ Move to the previous flow station
    end while
    $x_{NP} \leftarrow x$ ▷ Record the neutral point location
  end for
end for

After computing the neutral point (NP) location for all of the wave modes, we assemble the information the PSE requires for each mode: angular frequency, ω, streamwise wave number, α, spanwise wavenumber, β, and neutral point location, x_{NP}. The neutral point location may differ for each of the stability modes. If the base flow sustains both CF and TS modes, independent simulations are performed for these two mechanisms and the transition location is taken as the closest to the leading edge. We present further details on the relation between the lookup table, the LST, and the PSE codes in Sec. 3.6.

3.4 PSE Computation and Implementation Details

A fully-discrete version of Eq. (5) is obtained by applying Chebyshev differentiation matrices to the spatial derivatives in the wall-normal direction and replacing the streamwise coordinate derivative with a first or second-order backwards Euler marching scheme, in a way that x can be interpreted as a pseudo time. We map the Chebyshev matrices from the spectral space to a physical one, and the first and second order mapped Chebyshev matrices are named $\mathbf{D}_{1,\text{phys}}$ and $\mathbf{D}_{2,\text{phys}}$, respectively. Our boundary layer and PSE codes use distinct discretization schemes in the wall-normal direction, but share the same discretization in the streamwise direction. While the boundary layer code uses second-order finite differences in the wall-normal direction, the PSE module uses a high-order, spectral method based on Chebyshev collocation points. Therefore, a one-dimensional interpolation of the base flow states, $\bar{\mathbf{q}}$, is per-

formed between the two codes. We use cubic spline interpolation for this. The base flow information appears in the matrix operators for the PSE-based local, parallel problem and in the full nonparallel, nonlocal PSE as well.

Initial and boundary conditions are needed to close the marching procedure, as detailed in Sec. 2. The initial condition consists of an initial wave mode amplitude vector, $\hat{\mathbf{q}}_0$, and the streamwise wave number, α_0, and corresponds to the flow stability problem solution at the first marching station. As we focus on airfoil cases and on TS waves aligned with the inviscid streamline direction, $\beta = 0$. The angular frequency is not changed in the initial station iterative solution process, and the α value suggested by the database and LST codes is used as an initial guess for the first station solution, as detailed in Sec. 3.4. In the PSE module the user specifies the number of stations upstream of the neutral point where the initial station is to be located, with 2 to 4 stations being used in production runs to avoid the undesirable effects over the N-envelope computation reported by Langlois et al. [16], who showed that the N-factor curves can be incorrectly modified if a starting point is selected too far from the neutral point, potentially leading to a wrong transition onset location.

To determine the initial solution, we modify the original PSE equations to yield a local, parallel problem that is solved in the initial marching station. Therefore, we do not need to access a flow stability solution obtained from an external LST code. We modify the PSE operators defined in Eq. (5) to reflect the nature of a parallel problem. To do this, derivatives in the streamwise direction are excluded and the base flow velocity in this direction is set to zero. To obtain a local problem, meaning that the flow stability problem in each station is independent of the previous ones, we set the $\mathbf{D}$ matrix to zero, and Eq. (5) becomes:

$$\mathbf{A}_{p,l}\hat{\mathbf{q}} + \mathbf{B}_{p,l}\frac{1}{h_y}\frac{\partial \hat{\mathbf{q}}}{\partial y} + \mathbf{C}_{p,l}\frac{1}{h_y^2}\frac{\partial^2 \hat{\mathbf{q}}}{\partial y^2} = \mathbf{0}, \tag{20}$$

where the subscript p, l indicates the local, parallel solution obtained through the modified PSE equation. The discrete counterpart of Eq. (20) is,

$$\mathbf{A}_{p,l}\hat{\mathbf{q}}_1 + \frac{1}{h_y}\mathbf{B}_{p,l}\mathbf{D}_{1,\text{phys}}\hat{\mathbf{q}}_1 + \frac{1}{h_y^2}\mathbf{C}_{p,l}\mathbf{D}_{2,\text{phys}}\hat{\mathbf{q}}_1 = \mathbf{0}. \tag{21}$$

We solve Eq. (21) iteratively in an inexpensive way to avoid the computation of the entire eigenmode space that results from the solution of the local, parallel problem through a standard eigenvalue solver. We initialize $\hat{\mathbf{q}}_0$ as a zero vector and select both real and imaginary parts of α_0 as suggested by the database method. We modify the wall boundary conditions defined in Eqns. (6) and (7), leading to

$$\hat{u} = \hat{v} = \hat{T} = 0, \quad \hat{\rho} = 1 \quad \text{at} \quad y = 0, \tag{22}$$

$$\hat{u} = \hat{v} = \hat{w} = \hat{T} = 0 \quad \text{as} \quad y \to \infty, \tag{23}$$

and the wall condition for the wall normal component of the wave amplitude vector, $\hat{w} = 0$, is sought in the iterative process. Convergence is attained when $\hat{w}$ is close to zero up to a numerical tolerance of 2×10^{-8}. If $M < 0.5$, then the density fluctuations

are small and the boundary conditions specified in Eqns. (22) and (23) are modified to impose

$$\hat{u} = \hat{v} = \hat{T} = 0, \quad \frac{\partial \hat{u}}{\partial y} = 1 \quad \text{at} \quad y = 0, \tag{24}$$

$$\hat{u} = \hat{v} = \hat{w} = \hat{T} = 0 \quad \text{as} \quad y \to \infty, \tag{25}$$

where we specify a value for the wall-normal derivative of the streamwise velocity amplitude, $\hat{u}$. For both incompressible and compressible regimes, the choice of an inhomogeneous wall boundary condition to replace $\hat{w} = 0$ at the wall is required to respect the iterative process used in the local, parallel solution for the first marching station. In this sense, any small, non-zero number could be used in the wall inhomogeneous boundary condition. While solving the PSE-based local, parallel problem defined in Eq. (20), we update the streamwise wave number, α, using a secant method with the objective of driving $\hat{w}$ to zero at the wall,

$$\alpha_n = \alpha_{n-1} - \zeta\left(\alpha_{n-1}\right) \frac{\alpha_{n-1} - \alpha_{n-2}}{\zeta\left(\alpha_{n-1}\right) - \zeta\left(\alpha_{n-2}\right)}, \tag{26}$$

where $\zeta = \hat{w}$ at the wall and n is the iteration index. In the local, parallel problem, the growth rate defined in Eq. (10) is modified to account for the fact that the growth content is only present in the imaginary part of the streamwise wavenumber,

$$\sigma = -\alpha_i, \tag{27}$$

indicating that a negative imaginary part of α represents wave amplification.

With a converged solution for the first marching station, we have an initial condition to start the nonlocal, nonparallel PSE marching governed by Eq. (5). The marching is started following a first-order, implicit Euler scheme. We extend the first-order calculation up to the first ten marching stations to damp out transients arising from the local, parallel solution used in the first station. After that, a second-order, implicit marching scheme can be used. The key aspect of the PSE calculation is respecting the normalization condition defined in Eq. (8). As mentioned previously, the normalization condition is designed to remove fast streamwise variations present in the amplitude function, transferring them to the phase function. To enforce the normalization condition, we resort once more to the secant method defined in Eq. (27), using ζ as the integral defined in Eq. (8). In other words, we update the streamwise wavenumber, α, with the objective of driving the integral normalization condition to zero, with a convergence tolerance of 1×10^{-8}. This process highlights the fact that, in the PSE approach, the flow stability problem solution is obtained throughout an iterative computation at each marching station. Once convergence is attained for the present marching station, we move to the next one.

Capturing the decay of wall-normal wave amplitude components of typical TS waves requires the computational domain to extend beyond the boundary layer edge. A good practice to ensure that $\hat{w} = 0$ when $y \to \infty$ consists of checking how close $\hat{w}$ is to zero at the domain edge. For TS waves, we recommend a maximum wall-normal coordinate

in a given marching station to be as large as 100 to 150 times the boundary layer length scale, δ, in that flow section. For CF modes, the domain can be smaller than this. These numbers are valid as an initial guess for the domain size, and therefore we recommend the verification on the $\hat{w}$ decay towards zero as a systematic domain size check. In this sense, numerical experimentation has indicated that $\hat{w} = 1 \times 10^{-6}$ as $y \to \infty$ is a good compromise between accuracy and domain extension. To obtain the required base flow states beyond the boundary layer edge, we extrapolate the wall-normal velocity component, $\bar{w}$, using the value of its derivative at the boundary layer edge,

$$\bar{w}_{\text{ext}} = \bar{w}_{\text{e}} + \left.\frac{d\bar{w}_{\text{e}}}{dy}\right|_{e} (y - y_e)\,, \tag{28}$$

where the subscript e refers to the boundary layer edge and y is the wall-normal coordinate at the point of interest. For the base flow states other than the wall-normal velocity, the boundary layer edge quantities are directly used in the domain extending beyond the boundary layer itself.

In the marching process, we compute the disturbance growth rate as defined in Eq. (10). After the flow stability solution is obtained for all marching stations, the N-envelope for that specific wave mode is calculated. Details on the N-factor computation and the transition onset determination are presented in Sec. 3.5. The steps followed in the PSE calculation are summarized in Algorithm 2.

Algorithm 2 PSE computation

$\hat{\mathbf{q}}_1 \leftarrow \mathbf{0}$ ▷ Initialize local solution
$\alpha_1 \leftarrow \alpha_{DB}$ ▷ Initialize local wave number with database guess
while $\hat{w}_{\text{wall}} > 2 \times 10^{-8}$ **do**
    $\mathbf{A}_{p,l}\hat{\mathbf{q}}_1 + \frac{1}{h_y}\mathbf{B}_{p,l}\mathbf{D}_{1,\text{phys}}\hat{\mathbf{q}}_1 + \frac{1}{h_y^2}\mathbf{C}_{p,l}\mathbf{D}_{2,\text{phys}}\hat{\mathbf{q}}_1 = \mathbf{0}$ ▷ Solve the local, parallel PSE-based problem
    $\zeta \leftarrow \hat{w}_{\text{wall}}$
    $\alpha_n \leftarrow \alpha_{n-1} - \zeta\left(\alpha_{n-1}\right)\frac{\alpha_{n-1}-\alpha_{n-2}}{\zeta(\alpha_{n-1})-\zeta(\alpha_{n-2})}$ ▷ Use secant method to update the wave number
end while
$\Gamma \leftarrow 1 \times 10^{6}$ ▷ Initialize normalization condition to a large number
for i **in** n_{stations} **do**
    while $\Gamma > 1 \times 10^{-8}$ **do**
        $\mathbf{A}\hat{\mathbf{q}} + \frac{1}{h_y}\mathbf{B}\mathbf{D}_{1,\text{phys}}\hat{\mathbf{q}} + \frac{1}{h_y^2}\mathbf{C}\mathbf{D}_{2,\text{phys}}\hat{\mathbf{q}} + \mathbf{D}\frac{1}{h_x}\frac{\partial\hat{\mathbf{q}}}{\partial x} = \mathbf{0}$ ▷ Solve the nonlocal, nonparallel PSE problem
        $\Gamma \leftarrow \int_0^{\infty}\hat{\mathbf{u}}^{\dagger}\frac{\partial\hat{\mathbf{u}}}{\partial x}dy$ ▷ Compute the normalization condition
        $\zeta \leftarrow \Gamma$
        $\alpha_n \leftarrow \alpha_{n-1} - \zeta\left(\alpha_{n-1}\right)\frac{\alpha_{n-1}-\alpha_{n-2}}{\zeta(\alpha_{n-1})-\zeta(\alpha_{n-2})}$ ▷ Use secant method to update the wave number
    end while
    $\sigma \leftarrow \frac{1}{h_x}\left(-\alpha_i + \frac{d}{dx}\ln\sqrt{E(x)}\right)$ ▷ Compute the disturbance growth rate
end for
$N \leftarrow \int_{x_0}^{x}\sigma\left(x'\right)dx'$ ▷ Compute the N-factor for the wave mode under analysis

In this work, we refer to a disturbance growth rate through the generic variable σ. We use $-\alpha_i$ as a measure of disturbance growth in the local, parallel stability case represented by the LST formulation. In the spatial framework, $\alpha = \alpha_r + i\alpha_i$. In the LST method, the disturbance growth rate is $-\alpha_i$ due to the fact that there are no flow and disturbance variations in the streamwise direction, x. In the nonlocal, nonparallel case (PSE), the disturbance growth rate has also contributions from the streamwise variations. The disturbance kinetic energy based growth rate in the PSE approach, σ_E, is given by Eq. (10). It considers contributions from $-\alpha_i$ and from the disturbance kinetic energy variation in the streamwise direction. In Algorithm 2, the growth rate σ has the expression corresponding to σ_E (from PSE) assigned to it.

Our compressible PSE tool considers 2-D and quasi 3-D base flows with uniform or nonuniform meshes. Quasi 3-D base flows are characterized by the presence of a spanwise direction along which the flow states are nonzero and do not vary. The nomenclature 2.5-D is also used for this same flow topology. For instance, the flow far from the wing tip and root over a high aspect ratio swept wing can be seen as being 2.5-D. The stabilization procedure suggested by Andersson et al. [23] is included in the implementation. A growing mesh that emulates the boundary layer growth is included as an option. The number of elements inside the boundary layer is kept constant for all the flow stations. As a result, the spacing between elements increases in the wall-normal direction when moving downstream. Curvature metrics are included in the current implementation. Curvature effects are also introduced in the base flow quantities inside the PSE operators. Our PSE simulations based on the TS wave modes obtained by using the database method did not present unbounded amplification, indicating that spurious modes are not present in the process. A validation study is available in the literature [24].

3.5 N-factor and Transition Region Onset

The beginning of the transition region is determined based on an e^N method. The amplification factor, or N-factor, is defined as

$$N = \ln\left(\frac{A}{A_0}\right) = \int_{x_0}^{x} \sigma_E\left(x'\right) dx', \tag{29}$$

where A_0 is the disturbance amplitude at the first neutral-stability point. The N-factor envelope is obtained by running the PSE code using different frequencies and spanwise wave numbers, and superimposing the resulting N-factor curves at each station during the PSE solution. The transition to turbulence process starts as the N-factor reaches a critical threshold, N_{crit}.

The critical value for the N-factor, N_{crit}, is obtained from experimental data. For some transition mechanisms, empirical correlations are available. For TS waves, Mack [35] suggested correlating the critical N-factor to the turbulence level, Tu, using

$$N_{\text{crit,TS}} = -8.43 - 2.4\ln\left(Tu\right). \tag{30}$$

This correlation is valid for $0.001 < Tu < 0.01$. Critical N-factors for CF modes can also be obtained through a calibration process where experimental transition locations are known and flow stability analysis tools are used to determine $N_{\text{crit,CF}}$.

Mack's correlation was derived in conjunction with the LST theory and, currently, an equivalent relation developed based on a PSE approach is not available. However, this correlation has been used in conjunction with PSE analysis, in cases involving nonparallel effects and crossflow-driven transition [15]. In the airfoil flow problem we consider in this work, nonparallel effects retained in the PSE formulation do not play a major effect, making the use of Mack's correlation as a first approximation acceptable. Such effects are relevant when CF modes are considered [16].

3.6 Transition Prediction Framework

To compute the laminar boundary layer field, the boundary-layer solver uses the pressure coefficient (C_p) distribution as a boundary layer edge boundary condition. The pressure coefficient distribution at the laminar boundary layer edge can be obtained from different sources. A RANS solver can provide the required pressure distribution information. Inviscid formulation tools can also be used for this step if significant separation regions are not present in the flow field. For flows where no shock waves are present, such that the C_p distribution is not significantly affected by the transition location, no iterations in the transition location calculated are needed [24]. If shock waves are present, the impact of the transition location on the pressure distribution becomes non-negligible. In this case, it is necessary to feed back the pressure coefficient variations into the boundary layer solver, which uses it as a boundary condition. This impacts the base flow computation, which in turn has effects on the transition front computation. Therefore, flows that present a shock wave require an iterative procedure to determine the transition onset location.

The two-entry lookup table, that is embedded in the boundary layer solver, suggests a set of stability modes, comprising of wave numbers and angular frequencies, that are likely to drive the laminar base flow under consideration unstable. Our database method, described in Sec. 3.2, provides 20 TS wave modes to be used at the flow stability analysis level. The computation of the stability modes that should be processed in the PSE computation is, in general, a delicate step. Depending on the method used to obtain the stability modes, it is possible that spurious modes are obtained among the wave mode set. The spurious modes may lead to unbounded amplification, introducing errors in the N-envelope calculation used to detect the transition onset location. The presence of spurious modes requires the implementation of filters that are supposed to select only meaningful modes, increasing the computational cost. In our framework, we restrict ourselves to TS waves aligned with the external streamline direction. As suggested by Krumbein et. al. [19], the TS waves of interest for typical flight conditions are not off the inviscid streamline by large deflections. Our wave mode generation tool, based on the database method, completely avoids spurious modes while retaining the stability modes of physical relevance.

We choose to start the marching process some cells ahead of the neutral point, the user being able to choose the initial marching location, which may differ for each of the stability modes. To determine the neutral point for each wave mode, we use the LST solver, as described in Sec. 3.3. For a given mode, the computation starts at the unstable region, and an upstream marching detects the point of zero amplification,

corresponding to the neutral point. As highlighted in Algorithm 1, the unstable region is detected by inspecting the imaginary part of the streamwise wave number, α_i. We start in the first marching station and, when $\alpha_i < 0$, the unstable region is determined. For the TS-triggered transition case shown in this work, numerical experimentation indicated that all the wave modes involved in the N-envelope calculation present the same neutral point. This allows us to start the PSE computations at the same streamwise position for all the TS wave modes, making the process of automation easier. A further discussion on the effects of the starting point over the transition prediction results is available in Sec. 4.

The PSE computation, as detailed in Sec. 3.4, is carried out for all the stability modes suggested by the database method. The neutral point location is used to choose the starting marching location. As an initial step, the PSE operators, represented by the matrices $\mathbf{A}$, $\mathbf{B}$, $\mathbf{C}$, and $\mathbf{D}$ in Sec. 2, are assembled. In this step, we also build the Chebyshev differentiation matrices used to compute derivatives in the wall-normal direction. The marching process starts for each of the wave modes. The PSE solution involves the modes amplitudes, $\hat{\mathbf{q}}$, and the streamwise wave number, α. We advance to the next flow station after a convergence criterion is met. After respecting the normalization condition indicated in Eq. (8) at all streamwise positions, we use Eq. (10) to compute the growth rate at each streamwise location. Based on the wave growth rate, the N-factor is then computed for each of the wave modes using Eq. (29). The N-envelope is obtained for the set of waves used, and the transition location is determined from the critical N-factor, as illustrated in Sec. 3.5. The transition location as obtained by the PSE-e^N computation indicates the transition onset location. To enforce a transition region in the flow solver, a smooth intermittency function should be used. The detailed coupling between the CFD and transition solvers is available in the literature [24].

In summary, we use the numerical procedure highlighted in Sec. 3.4 to compute the disturbance growth rate, σ, for a collection of stability modes suggested by the database method. The amplification factor, N, is computed for each of the stability modes following the mathematical relations introduced in Sec. 3.5. The procedure is repeated for all stability modes and an N-envelope is built. The transition onset location is then determined according to the procedure described in Sec. 3.5. Our strategy to determine the transition onset location is robust, avoiding the presence of spurious stability modes. The framework we propose is suitable for automation and, therefore, compatible with industry practices.

4 Numerical Results

The Natural Laminar Flow NLF(1)-0416 airfoil is a general aviation airfoil tested at the NASA Langley Low-Turbulence Pressure Tunnel [36]. For the selected flight condition, the chord-based Reynolds number is 4×10^6 and the Mach number is 0.1, at a zero degree angle of attack. Experimental data [36] suggest that transition is triggered by amplification of TS waves on the airfoil suction in this flight condition. The turbulence intensity was not measured during this test, but separate measurements in

the same facility indicated that it is a quiet wind tunnel [37]. Using the Approximate Amplification Factor Transport (AFT) transition model, Coder [38] observed that the value of $Tu = 0.045\%$, corresponding to $N_{\text{crit,TS}} = 10.07$ as reported in Ref. [37], leads to transition fronts upstream of the measured [36] locations for an angle of attack sweep at a chord-based Reynolds number of 4×10^6. Coder found improved agreement between the AFT simulations and measurements for $Tu = 0.15\%$, corresponding to $N_{\text{crit}} = 7.18$ [38]. For the PSE-based transition prediction presented here, we chose $Tu = 0.1\%$ as a best guess, with a corresponding critical $N_{\text{crit,TS}} = 8.14$ per Eq. (30). This choice is based on the spread observed in the turbulence intensity for this test case. Based on the knowledge that the wind tunnel is quiet, we believe that $Tu = 0.1\%$ represents a good compromise between the freestream turbulence intensity levels mentioned above. We also investigate the freesteam turbulence intensity level that leads to an exact transition location match. A discussion of this is presented further in this section.

The boundary conditions used in this test case are those indicated in Eqns. (6), (7), (22), and (23). The boundary layer solver uses the pressure coefficient distribution from a RANS, Euler, or potential flow solver as the freestream boundary condition.

The NLF(1)-0416 computational mesh has 100 Chebyshev nodes in the wall-normal direction for both suction and pressure sides of the airfoil. The mesh has point clustering close to the wall to capture the wave mode activity in the near-wall region and the computational domain grows in the marching direction to capture boundary layer growth effects. Suitable mappings between the Chebyshev and physical spaces for incompressible and compressible flows are available in the literature [39, 40]. In some situations, it may be useful to coarsen the boundary layer mesh in the streamwise direction to perform the PSE analysis to avoid numerical instability effects, as mentioned in Sec. 2. For the NLF(1)-0416 simulations, we use the same streamwise discretization in the boundary layer and PSE modules, the number of elements in the streamwise direction for the PSE analysis being dependent on the neutral point location.

Following the PSE-based transition prediction framework detailed in Secs. [3.4]-[3.5], we start by inspecting the flow stability modes suggested by the database method for the selected flight condition. The flow stability analysis is performed for the suction and pressure sides of the airfoil separately, and the stagnation point is used as the geometric location where the splitting is performed.

We use three distinct meshes to investigate the PSE solution corresponding to the flow on the airfoil suction side. The coarse mesh presents 27 stations in the flow direction and 50 Chebyshev nodes in the wall normal direction, representing a total of $N_{\text{elements}} = 1350$ elements. The baseline mesh consists of 54 stations in the streamwise direction and 100 Chebyshev points in the wall-normal direction, for a total of $N_{\text{elements}} = 5400$. Finally, the fine mesh shares the streamwise discretization with the baseline one, but doubles the number of Chebyshev points to 200, with a total number of elements of $N_{\text{elements}} = 10800$. A further increase in the number of points in the streamline direction would make the PSE marching procedure unstable, as mentioned in Sec. 2. The normalized absolute value of the wall-normal wave velocity component, $\hat{w}$, at the mid-station position corresponding to $(x/c) = 0.58$ is plotted against the wall-normal coordinate for the three meshes in Fig. 2, which also includes the

predicted transition location, $(x/c)_{\text{tr}}$, for the three computational meshes.

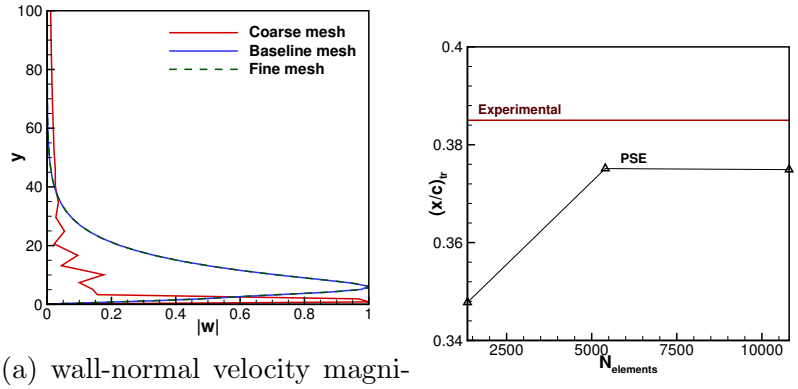

(a) wall-normal velocity magnitude

(b) transition location

Figure 2: Mesh refinement impact over wall-normal normalized wave velocity (left, complex number magnitude) and $(x/c)_{\text{tr}}$ (right) for the suction side.

The coarse mesh leads to an eigenfunction solution for $\hat{w}$ that presents an unphysical, oscillatory behavior close to the wall. The coarse mesh also does not attain the $\hat{w} \to 0$ boundary condition as $y \to \infty$ with the required accuracy. The predicted transition location is upstream of the experimental location by 9.67%. The flow solutions for the baseline and the fine mesh are numerically equivalent to machine precision, and therefore the results corresponding to the baseline mesh are considered mesh-independent. This mesh serves as the standard for all numerical results presented in this paper. We also observe that the baseline and fine meshes allow $\hat{w} \to 0$ as $y \to \infty$, respecting the fact that the flow disturbance may vanish away from the wall. The transition location for the baseline and fine meshes is $(x/c)_{\text{tr}} = 0.375$, which is within 2.56% of the experimental value, $(x/c)_{\text{tr,exp}} = 0.385$. As mentioned in Sec. 3, we recommend a maximum wall-normal coordinate in a given marching station to be as large as 100 to 150 times the boundary layer length scale, δ, in that section. In the results shown in Fig. 2, we use $y = 100\delta$, assuring that the computational domain is large enough to allow a smooth eigenfunction decay outside of the boundary layer. If the domain does not extend sufficiently beyond the boundary layer edge, then the eigenfunctions present a sharp profile as $y \to \infty$, therefore not obeying the expected physical behavior in that region.

The initial wave modes suggested by the database method are depicted in Fig. 3 for the suction (left) and pressure (right) sides of the airfoil. The real and imaginary parts of the streamwise wavenumber, α, are normalized by the boundary layer characteristic length scale, δ, evaluated at the neutral point location. The dimensional frequencies for each of the wave modes are also indicated in Fig. 3.

The non-dimensional angular frequency, ω, is related to the dimensional frequency, f (in Hertz), as follows,

$$\omega = 2\pi Re_0 f \left(\nu_0 / U_{e,0}^2\right), \tag{31}$$

where Re follows the definition presented in Sec. 2, and subscripts 0 and e indicate the neutral point and the boundary layer edge, respectively. The wave modes triggering

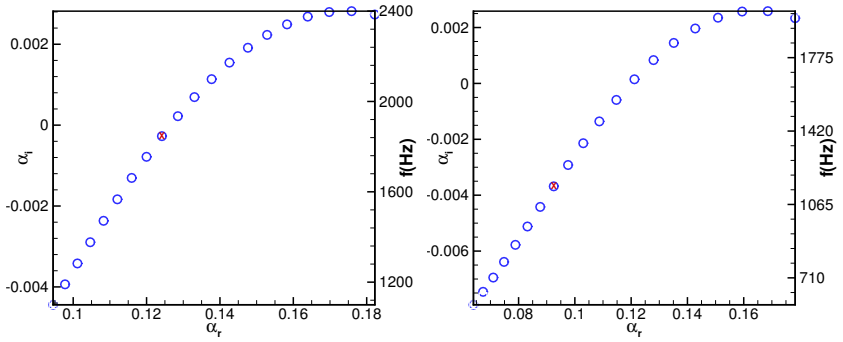

(a) Suction side (b) Pressure side

Figure 3: Database, initial wave modes for the NLF(1)-0416 airfoil.

transition for both suction and pressure sides are marked with a red symbol. As we consider TS waves aligned with the external streamline direction, $\beta = 0$. Our LST code suggests that the neutral point is located at $x/c = 0.16$ for the airfoil suction side in this work. For the airfoil pressure side, the neutral point is located at $x/c = 0.14$ for all TS wave modes. We start our PSE computation by solving a PSE-based local, parallel problem, as detailed in Sec. 3.4. Numerical experimentation indicated that the local problem used to start the PSE marching should be solved two flow stations upstream of the neutral point location. This is in agreement with results available in the literature [16]. Since the starting point is only two cells away from the neutral point, the PSE-based local, parallel problem computes a converged streamwise wave number, α, whose real part is close to the one suggested by the database method as the initial guess. For instance, for the airfoil suction side, the initial guess is $\alpha = 0.1242 - 2.7250 \times 10^{-4} i$ and the converged value from the local, parallel problem is $\alpha = 0.1233 + 2.4835 \times 10^{-3} i$. The imaginary part of α indicates amplification or damping, with a small absolute value representing the neutral point. In the values for α exemplified above, a negative imaginary part represents wave growth, as indicated in Sec. 3.4. For the database guess and the converged local, parallel problem result we observe that the absolute value of α_i is close to zero, indicating a neutral point location.

The normalized velocity eigenfunctions in the mid-station for the NLF(1)-0416 airfoil are illustrated in Fig. 4. Since the NLF(1)-0416 airfoil is a subsonic design, the density and temperature eigenmodes are not plotted in Fig. 4, even though they are part of the solution because our PSE implementation follows a compressible formulation. Inspection of the eigenmodes as $y \to \infty$ indicates that the boundary conditions in Eqns. (6) and (7) are attained without unphysical variations close to the domain boundaries. If the computational domain does not extend in the wall-normal direction as suggested in Sec. 3.4, the eigenmodes decay abruptly to zero as $y \to \infty$ to respect the imposed boundary conditions, not representing the physics observed in the decaying solution modes.

Disturbance growth rates for the suction and pressure sides of the NLF(1)-0416 airfoil are depicted in Fig. 5. The x/c location corresponding to $\sigma = 0$ corresponds to the neutral point, beyond which amplification starts to occur. TS waves are amplified

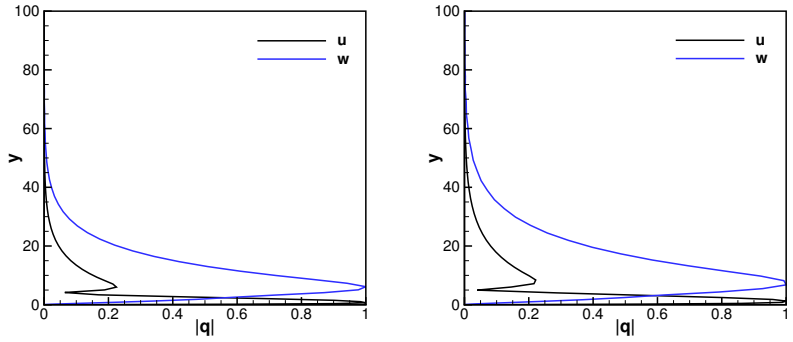

(a) Suction side (b) Pressure side

Figure 4: Normalized absolute values of eigenfunctions in the mid-station for the NLF(1)-0416 airfoil.

by adverse pressure gradients. The presence of adverse pressure gradients in the suction side of the NLF(1)-0416 airfoil results in growth rates that are larger than those seen in the pressure side, leading to transition to turbulence earlier in the former.

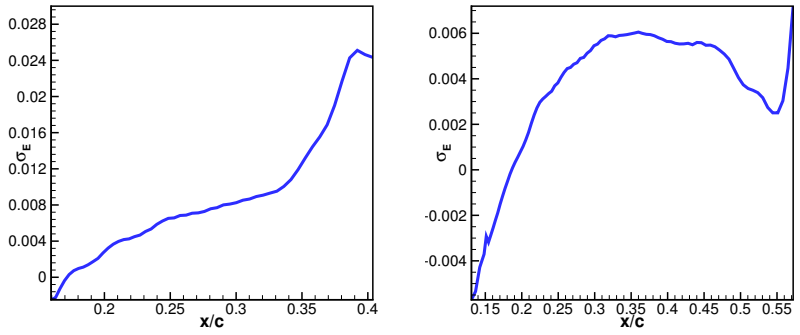

(a) Suction side (b) Pressure side

Figure 5: Disturbance growth rates for the NLF(1)-0416 airfoil.

The N-envelopes corresponding to the selected flight condition are represented in Fig. 6, adapted from Ref. [24]. The transition onset locations are determined according to the procedure outlined in Sec. 3.5. Table 1 lists the numerical and experimental transition locations for this test case. The numerical results indicate a good agreement with experimental data and highlight that using $Tu = 0.1\%$ is a good choice for this specific test case when using PSE to predict transition. It was found that a critical

Table 1: Transition onset locations for the NLF(1)-0416 airfoil. PSE.

Side	PSE, $(x/c)_{tr}$	Experiment, $(x/c)_{tr}$ [36]	Difference (%)
Upper	0.375	0.385	2.56
Lower	0.497	0.525	5.33

N-factor of $N_{\text{crit,TS}} = 9.3$ needs to be used in the computations to match the transition

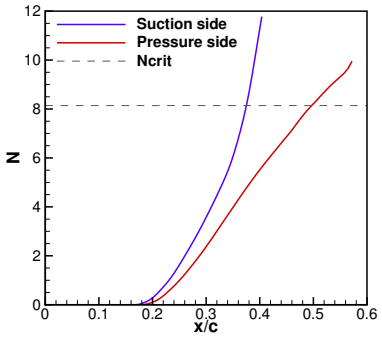

Figure 6: N-factor envelopes for the selected condition [24].

location measured in the experiments. This corresponds to $Tu = 0.062\%$. This result suggests that a calibration of Mack's correlation for use with nonlocal, nonparallel flow stability tools may be an interesting research line. If $Tu = 0.15\%$ is used as in Ref. [38], the suction side transition front is located at $(x/c)_{\text{tr,up}} = 0.365$, while the pressure side transition front is predicted to be at $(x/c)_{\text{tr,up}} = 0.461$. This represents errors of 5.2% and 12.2% for the suction and pressure sides, respectively. To compare the PSE and LST approaches, we use the LST code to predict the transition front for this test case. The local, parallel results also present good agreement with experimental data, but the errors are larger than those corresponding to the PSE simulations. Results based on the LST computations are shown in Table 2.

Table 2: Transition onset locations for the NLF(1)-0416 airfoil. LST.

Side	LST, $(x/c)_{tr}$	Experiment, $(x/c)_{tr}$ [36]	Difference (%)
Upper	0.404	0.385	4.93
Lower	0.565	0.525	7.62

We investigate the effects of the starting marching position over the energy-based growth rates σ_E, and N-factor envelopes for the upper airfoil side. We select the TS wave mode that triggers transition for this test case, corresponding to the mode marked with a red cross in the left plot of Fig. 3. For this case, the neutral point is located at $x/c = 0.16$. Results shown in Fig. 7 (left) illustrate the energy-based growth rate behavior for starting points located 5 and 2 stations upstream of the neutral point, at the neutral point itself, and 5 stations downstream of the neutral point. Small differences among the growth rate curves are observed. The initial database method guess for the streamwise wave number, α, corresponds to the neutral point location. If the marching location is chosen close to the neutral point, in our case within 5 stations upstream or downstream of it, the parallel, local problem converges to an α value close enough to the original guess so that the computational results are not greatly impacted by the starting location. This is further verified by observing the impact of the starting marching station over the resulting N-factors, with results illustrated in Fig. 7 (right). The N-factors shown here correspond to the amplification factor for the TS wave mode

that triggers transition, different from the N-envelopes shown in Fig. 6. We observe that the impact of the starting point on the N-factor curves is even less noticeable than what is observed for the growth rates. When the N-factor is computed, integration per Eq. (29) filters out the effects of the starting point that would be noticed in previous stages of the computational process. The transition locations corresponding to the distinct starting points are given in Table 3. The PSE-based transition onset point are compared to the experimental result, $(x/c)_{\text{tr,exp}} = 0.385$. For all the starting points, the error is within 2.6% of the experimental data, indicating that the starting point selection has no impact on the predicted transition front as long as it lies close to the neutral point.

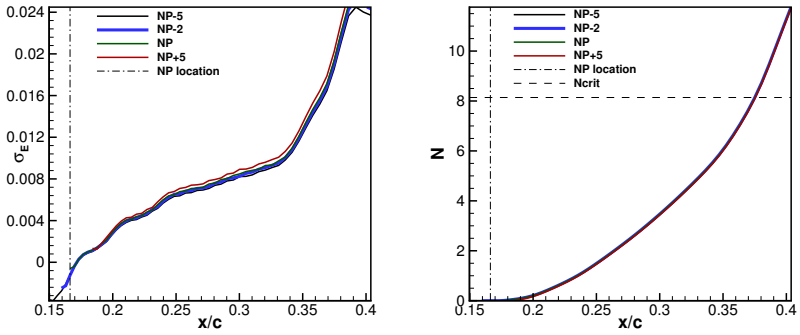

(a) Energy-based growth rate (b) N-factor

Figure 7: Energy-based growth rate and N-factor for distinct starting positions for the suction side.

Table 3: NLF(1)-0416 airfoil transition points.

Starting position	$(x/c)_{tr}$	Difference from experimental results (%)
NP-5	0.3753	2.5317
NP-2	0.3751	2.5654
NP	0.3752	2.5388
NP+5	0.3756	2.4335

5 Conclusions

Airplane manufacturers are currently directing efforts towards greener, more fuel-efficient aircraft. Aerodynamic design plays a vital role in reducing fuel consumption through drag reduction. Laminar boundary layers introduce less viscous drag when compared to turbulent ones. This is especially true at cruise conditions, where flow separation is likely limited to small regions of the airframe.

Fully-turbulent computational fluid dynamics (CFD) solvers must be augmented with transition to turbulence prediction for benefit from laminar flow technologies to

be realized. The parabolized stability equations (PSE) retain nonparallel and nonlocal effects that are typical of boundary layers. Therefore, the PSE approach has a higher fidelity than the widely used linear stability theory (LST) approach. The computational cost of a PSE solution is similar to the one associated with an LST computation. However, since it first appeared in the late nineties, the PSE method has not been adopted as a tool in industrial environments, in part due to difficulties in the method set up and implementation.

To address the initialization issues and to make the PSE approach more compatible with industry requirements, we propose a robust initialization process. We use a database method to select the flow stability modes that are used with the PSE computations leading to the transition onset location. TS waves aligned with the external streamline direction are used in our computations. Our transition prediction framework is also able to address stationary CF vortices. In three-dimensional configurations, the marching procedure can be performed along a direction normal to the leading edge or over the external streamline direction. Future studies will investigate this transition mechanism in detail. Our database method approach generates a set of TS waves that do not include spurious modes. It is computationally inexpensive, and is shown to be robust. The neutral point is computed by using a linear stability theory (LST) solver that performs an upstream marching to select the neutral point for each of the stability modes. To make this possible, we eliminate the nonparallel terms of a standard PSE computation. We also turn off nonlocal effects. With flow stability modes and corresponding neutral points determined, the PSE computation is performed. Our framework facilitates the use of the PSE technique in industry environments and therefore represents an important initial step on the way to a full industrialization of the approach in the future. For the PSE computation, nonlocal and nonparallel terms are included. The simulation is processed through marching, using the local, parallel problem mentioned above as the starting point. In our production runs, we choose to start the marching 2 cells ahead of the neutral point, even though results presented in this paper indicate that a starting point placed anywhere between 5 cells upstream and 5 cells downstream of the neutral point results in transition front locations that are within 2.56% of the reported experimental data for the subsonic airfoil tested here. The nonlocal, nonparallel marching can be performed using both first and second-order accurate implicit Euler schemes. The domain size must be such that the wave amplitude vanishes away from the wall, and the mesh refinement must assure the correct computation of the wave amplitude profiles while respecting the stability bounds that are inherent to the PSE calculation.

Numerical results for the NLF(1)-0416 airfoil illustrate the transition prediction framework proposed in this paper. We present the TS wave modes suggested by the database method as candidates for triggering transition for the NLF(1)-0416 airfoil. The resulting eigenfunctions are also illustrated. Growth-rates and N-factor results are reported. The predicted transition onset points show agreement with experimental data. The numerical results presented in this paper are based on a freesteam turbulence intensity level of $Tu = 0.1\%$, which corresponds to $N_{\mathrm{crit,TS}} = 8.14$, for which the predicted transition locations are within 5.5% of the experimental data. The turbulence intensity for the wind tunnel test section is reported to be $Tu = 0.045\%$, which leads

to $N_{\mathrm{crit,TS}} = 10.07$. Numerical experimentation also indicated that, when using PSE, the best match with experimental data corresponds to $Tu = 0.062\%$, or $N_{\mathrm{crit,TS}} = 9.3$. This suggests that additional $N_{\mathrm{crit,TS}}$ empirical correlations would be welcomed. It is also relevant to further investigate how distinct flow stability tools, when used with an e^N method, will require specific empirical correlations. For flow topologies for which nonparallel effects and crossflow modes are relevant, as in the vicinity of a leading edge, further validation using adapted empirical transition threshold correlations will be needed.

When compared to modified RANS models that consider transition to turbulence, as the amplification factor transport (AFT) and the Langtry–Menter (LM) models, the PSE approach presents a smaller level of modeling dependence. This is because the stability modes are directly computed, and the modeling limitations are only related to the hypotheses that underly the method. On the other hand, in modified RANS models that encapsulate transition effects, transport equations that mimic the transition phenomena are added to an underlying turbulence model, and tracking the direct stability mode evolution is therefore not an objective. This makes this type of transition module more versatile and suitable for applications in a broader range of studies. For instance, flow stability tools will detect the evolution of both TS and CF modes without the need to modify the governing equations, as is the case for RANS models. Additionally, the stronger dependence on the empirical data that are used to build the source terms in the RANS models makes their effectiveness for situations where the flow topology deviates from the ones used to build the empirical correlations uncertain. Modified RANS models, on the other hand, have shown good agreement with experimental data for the flow conditions that are part of the data used to derive the correlations that are part of their formulations. These models have the benefit of being completely nested in the CFD solver, not requiring an external module. Therefore, we believe that PSE-based transition tools and modified RANS models that consider transition have both a place in both academic and industry environments and can be said to complement each other.

Future work should address a closer comparison between LST and PSE approaches when used along with an e^N method to predict transition over typical aircraft configurations. Available results in the literature indicate that the inclusion of nonparallel effects, which are considered in the PSE approach, may provide better agreement with experimental data in some situations. One example is CF-triggered transition to turbulence, which typically happens over swept wings at high Mach and Reynolds numbers conditions. Geometries that present high curvatures may also benefit from a PSE-based transition prediction because curvature effects are not compatible with the LST approach. Future investigations should also address the CF-triggered transition mechanism. The transition framework presented here presents the first step towards a fully-automatic, PSE-based transition prediction tool. Further work will investigate flow conditions that consider TS, CF, and mixed TS-CF stability modes. This further work will expand the transition prediction framework presented here and make it compatible with industry requirements.

Acknowledgments

The authors gratefully acknowledge the support provided by Conselho Nacional de Desenvolvimento Científico e Tecnológico, CNPq, Brazil, under Research Grant No. 205552/2014-5. The authors thank Prof. Ardeshir Hanifi (KTH) and Dr. Márcio Teixeira de Mendonça (Instituto de Aeronáutica e Espaço) for the insightful discussions on the PSE approach. We also thank Yayun Shi for the discussions on the database and LST approaches.

References

[1] Crouch, J. D., "Boundary-Layer Transition Prediction for Laminar Flow Control," AIAA Paper No. 2015-2472*, Proceedings of the 45th AIAA Fluid Dynamics Conference*, AIAA, Dallas, TX, June 2015.

[2] Krishnan, K. S., Bertram, O., and Seibel, O., "Review of Hybrid Laminar Flow Control Systems," *Progress in Aerospace Sciences*, Vol. 93, No. February, 2017, pp. 24–52.

[3] Schrauf, G. H. and von Geyr, H., "Simplified Hybrid Laminar Flow Control for the A320 Fin - Aerodynamic and System Design, First Results," AIAA Paper No. 2020-1536*, Proceedings of the AIAA Scitech 2020 Forum*, Orlando, FL, January 2020.

[4] Schrauf, G., "Key Aerodynamic Technologies for Aircraft Performance Improvement," *Fifth Community Aeronautical Days*, June 2006.

[5] Schlichting, H. and Gersten, K., *Boundary-Layer Theory*, Springer, Boston, 2003.

[6] Halila, G. L. O., Antunes, A. P., Silva, R. G., and Azevedo, J. L. F., "Effects of Boundary Layer Transition on the Aerodynamic Analysis of High-lift Systems," *Aerospace Science and Technology*, Vol. 90, July 2019, pp. 233–245.

[7] Reed, H. L., Saric, W. S., and Arnal, D., "Linear Stability Theory Applied to Boundary Layers," *Annual Review of Fluid Mechanics*, Vol. 28, January 1996, pp. 389–428.

[8] Reed, H., Saric, W., and White, E., "Stability and Transition of three-dimensional Boundary Layers," *Annual Review of Fluid Mechanics*, Vol. 35, January 2003, pp. 413–440.

[9] Saric, W. S., "Introduction to Linear Stability," Advances in laminar turbulent transition modeling. the lecture series of the von karman institute, 2008.

[10] Smith, A. M. O. and Gamberoni, N., "Transition, Pressure Gradient and Stability Theory," Douglas Aircraft Company Report ES 26388, Douglas Aircraft Company, Long Beach, CA, 1956.

[11] van Ingen, J. L., "A Suggested Semi-Empirical Method for the Calculation of the Boundary Layer Transition Region," Univ. Delft Report VTH-74, University of Delft, Delft, The Nederlands, 1956.

[12] Arnal, D., "Practical Transition Prediction Methods: Subsonic and Transonic Flows," Advances in Laminar Turbulent Transition Modeling. The Lecture Series of the von Karman Institute, 2008.

[13] Bertolotti, F. P. and Herbert, T., "Analysis of the Linear Stability of Compressible Boundary Layers using PSE," *Theoretical and Computational Fluid Dynamics*, , No. 3, 1991, pp. 117–124.

[14] Herbert, T., "Parabolized Stability Equations," *Annual Review of Fluid Mechanics*, Vol. 29, 1997, pp. 245–283.

[15] Kosarev, L., Séror, S., and Lifshitz, Y., "Parabolized Stability Equations Code with Automatic Inflow for Swept Wing Transition Analysis," *Journal of Aircraft*, Vol. 53, No. 6, November-December 2016, pp. 1647–1669.

[16] Langlois, M., Casalis, G., and Arnal, D., "On the Practical Applications of the PSE Approach to Linear Stability Analysis," *Aerospace Science and Technology*, Vol. 2, No. 3, March-April 1998, pp. 167–176.

[17] Perraud, J., Arnal, D., Casalis, G., Archambaud, J.-P., and Donelli, R., "Automatic Transition Predictions Using Simplified Methods," *AIAA Journal*, Vol. 47, No. 11, 2009, pp. 2676–2684.

[18] Shi, Y., Gross, R., Mader, C. A., and Martins, J. R. R. A., "Transition Prediction Based on Linear Stability Theory with the RANS Solver for Three-Dimensional Configurations," *Proceedings of the AIAA Aerospace Sciences Meeting, AIAA SciTech Forum*, Kissimmee, FL, January 2018.

[19] Krumbein, A., Krimmelbein, N., Grabe, C., and Shengyang, N., "Development and Application of Transition Prediction Techniques in an Unstructured CFD Code (Invited)," *Proceedings of the AIAA AFluid Dynamics Conference, AIAA Aviation Forum*, Dallas, TX, June 2015.

[20] Bertolotti, F. P., *Turbulence and Transition Modelling. Ch. 8, Transition Modelling based on the PSE*, Kluwer Academic Publishers, Netherlands, 1996.

[21] Hanifi, A., Henningson, D., Hein, S., Bertolotti, F., and Simen, M., "Linear Nonlocal Instability Analysis - the linear NOLOT code," The Aeronautical Research Institute of Sweden Aerodynamics Department, FFA-TN 1994-54, 1994.

[22] Juniper, M. P., Hanifi, A., and Theofilis, V., "Modal Stability Theory. Lecture notes from the FLOW-NORDITA Summer School on Advanced Instability Methods for Complex Flows. Stockholm, Sweden, 2013," *Aplied Mechanics Reviews*, Vol. 66, March 2014, pp. 1–22.

[23] Andersson, P., Henningson, D. S., and Hanifi, A., "On a Stabilization Procedure for the Parabolic Stability Equations," *Journal of Engineering Mathematics*, Vol. 33, February 1998, pp. 311–332.

[24] Halila, G. L. O., Chen, G., Shi, Y., Fidkowski, K. J., Martins, J. R. R. A., and de Mendonça, M. T., "High-Reynolds Number Transitional Flow Simulation via Parabolized Stability Equations with an Adaptive RANS Solver," *Aerospace Science and Technology*, Vol. 91, August 2019, pp. 321–336.

[25] Chang, C. L., "LASTRAC.3d: Transition Prediction in 3D Boundary Layers," AIAA Paper No. 2004-2542*, Proceedings of the 34th AIAA Fluid Dynamics Conference and Exhibit*, Portland, OR, June 2004.

[26] KAUPS, K. and CEBECI, T., "Compressible laminar boundary layers with suction on swept and tapered wings," *Journal of Aircraft*, Vol. 14, No. 7, 1977, pp. 661–667.

[27] Cebeci, T., *Stability and Transition: Theory and Application. Efficient Numerical Methods with Computer Programs*, Heidelberg, Springer-Verlag Berlin Heidelberg, 2004., Berlin, 2004.

[28] Shi, Y., Mader, C. A., He, S., Halila, G. L. O., and Martins, J. R. R. A., "Natural Laminar Flow Airfoil Design Using a Discrete Adjoint Approach with RANS-eN Transition Prediction," *AIAA Journal*, 2020, (Submitted).

[29] Golbabai, A. and Javidi, M., "Newton-Like Iterative Methods for Solving System of Non-Linear Equations," *Applied Mathematics and Computation*, Vol. 192, No. 2, 2007, pp. 546–551.

[30] Arnal, D., "Transition Prediction In Transonic Flow," *IUTAM Symposium Transsonicum III DFVLR-AVA*, 1988, pp. 253–262.

[31] White, F. M., *Viscous Fluid Flow*, McGraw-Hill, New York, NY, 1991.

[32] Malik, M. R. and Orszag, S. A., "Linear Stability Analysis of Three-Dimensional Compressible Boundary Layers," *Journal of Computational Physics*, Vol. 2, March 1987, pp. 77–97.

[33] Bai, Z., Demmel, J., Dongarra, J., Ruhe, A., and van der Vorst, H., *Templates for the Solution of Algebraic Eigenvalue Problems: A Practical Guide*, SIAM, Philadelphia, 2000.

[34] Gaster, M., "A Note on the Relation between Temporally-Increasing and Spatially-Increasing Disturbances in Hydrodynamic Stability," *Journal of Fluid Mechanics*, Vol. 14, No. 2, 1962, pp. 222–224.

[35] Mack, L. M., "Transition Prediction and Linear Stability Theory," AGARD Report CP224, 1977.

[36] Somers, D. M., "Design and Experimental Results for a Flapped Natural-Laminar-Flow Airfoil for General Aviation Applications," Tech. rep., NASA Langley Research Center, Hampton, VA, United States, 1981, NASA-TP-1865, L-14409, NAS 1.60:1865.

[37] von Doenhoff, A. E. and Abbott, F. T., "The Langley Two-Dimensional Low-Turbulence Pressure Tunnel," NACA TN-1947-1283, NACA, May 1947.

[38] Coder, J. G., *Development of a CFD-Compatible Transition Model Based on Linear Stability Theory*, Ph.D. thesis, The Pennsylvania State University, State College, PA, 2014.

[39] Malik, M. R., Zang, T., and Hussaini, M., "A Spectral Collocation Method for the Navier–Stokes Equations," *Journal of Computational Physics*, Vol. 61, Oct. 1985, pp. 64–88.

[40] Malik, M. R., "Numerical Methods for Hypersonic Boundary Layer Stability," *Journal of Computational Physics*, Vol. 86, February 1990, pp. 376–413.